

Charge-carrier transport simulations in diamond detectors with electric-field-dependent mobility and charge-collection-distance-based trapping

Faiz Rahman Ishaqzai^{*1,2}, Muhammed Deniz², Marta Baselga¹, Tobias Bisanz¹, Kevin Kröniger¹, Jens Weingarten¹, and Antonia Wippermann¹

¹*TU Dortmund University, Dortmund, Germany*

²*Department of Physics, Dokuz Eylül University, Buca, İzmir TR35160, Türkiye*

^{*}*faiz.ishaqzai@tu-dortmund.de*

March 16, 2026

Abstract

Diamond detectors are attractive for operation in harsh radiation environments because they combine radiation tolerance, fast signal formation, and low leakage current. Realistic detector-response simulations require an accurate description of charge-carrier mobility and trapping, which determine both signal amplitude and timing. In this work, we extend Allpix Squared, a modular end-to-end detector simulation framework, with diamond-specific transport models. The implementation includes field-dependent mobility parameterizations for electrons and holes and an effective trapping model based on the charge collection distance (CCD), providing a detector-level interface to material quality and radiation-damage measurements. The mobility description is validated in the negligible-trapping limit using single-crystalline CVD diamond by comparing simulated drift velocities and transient-current signals with published reference data. For polycrystalline CVD diamond, the CCD-based trapping model is evaluated using experimentally measured CCD values and compared with laboratory transient-current-technique waveforms. The simulations reproduce the measured drift-velocity behavior in scCVD and the reduced charge collection and degraded transient response observed in pcCVD. The presented implementation enables detector-level studies of charge collection, pulse formation, and timing performance in diamond sensors using experimentally accessible transport and trapping parameters, and provides a practical framework for simulation-driven detector development and radiation-damage studies.

Keywords: Diamond detector; Allpix Squared; Charge transport; Mobility; Trapping; Charge collection distance; Transient current technique

Contents

Abstract	1	3.3.3 Event selection	6
1 Introduction	1	3.3.4 Mean waveform and Transient Times	6
2 Mobility and trapping models	2	4 Simulations and Results	7
2.1 Mobility models	2	4.1 scCVD mobility validation	7
2.2 Trapping Model	2	4.1.1 Electrons (PW model)	7
3 Experimental setups and measurements	3	4.1.2 Holes (CT model)	8
3.1 Electrical Measurements	3	4.2 pcCVD CCD/trapping validation	8
3.1.1 Current-voltage characteristics	3	5 Conclusions and outlook	11
3.1.2 Capacitance-voltage profiles	4	1 Introduction	
3.2 CCD/CCE measurements	4	Diamond sensors are an attractive option for particle detection in harsh operating conditions, in particular in environments combining high radiation fluence, high particle rates, and demanding timing requirements [1–3]. Their performance is governed by charge carrier mobility and charge carrier trapping, which together determine the signal size and timing response [4,5].	
3.2.1 Experimental setup and readout chain	4	Accurate detector simulations are essential to translate material-level models into detector parameters or vice versa in order to support real-world detector design. Allpix Squared is a modular, end-to-end simulation framework	
3.2.2 Data acquisition	4		
3.2.3 Offline pulse-height (charge) reconstruction	4		
3.2.4 Event selection (cuts)	5		
3.2.5 Charge calibration, MPV extraction, and CCD	5		
3.3 Transient Current Measurements	6		
3.3.1 Experimental setup and readout chain	6		
3.3.2 Data Acquisition	6		

arXiv:2603.13146v1 [physics.ins-det] 13 Mar 2026

for semiconductor tracking and vertex detectors, providing a configurable chain from energy deposition (via Geant4) to charge transport and digitized detector response [6]. It provides access to detector-level observables, e.g. the collected charge, the signal pulse shape as well as timing information, making it an indispensable tool for studying the impact of material properties on semiconductor detector operation. Its modular architecture allows the implementation of transport models and material descriptions for other semiconductors than silicon.

In this work, we present an implementation of chemical vapor deposition (CVD) diamond as a sensor material in Allpix Squared where we place an emphasis on two ingredients required for realistic detector-response simulations. First, we introduce field-dependent mobility models for electrons and holes to describe drift velocity, impacting charge collection time, time resolution, and charge sharing. Second, we implement an effective trapping description expressed through the charge collection distance (CCD), which directly links to the collected charge and provides a convenient interface to polycrystalline structures and radiation-damage measurements.

We distinguish two practically relevant scenarios. For an unirradiated single-crystalline CVD diamond (scCVD), we validate the field-dependent mobility model in the negligible-trapping limit, where charge collection distance is consistent with the sensor thickness under typical operating voltages. For poly-crystalline CVD diamond (pcCVD), we assume the same mobility parameterization, which has been shown to be a good approximation [7] and model signal loss with an effective trapping description, quantified by supplying the charge-collection distance (CCD) as an external input.

The remainder of this paper is organized as follows. [Section 2](#) introduces the mobility and trapping models, and describes their implementation in Allpix Squared. [Section 3](#) summarizes the reference datasets, experimental setups and comparison procedure. [Section 4](#) presents results for the validation of the implementation of mobility and trapping models. The study is concluded in [Section 5](#).

2 Mobility and trapping models

In this section, we introduce the mobility and trapping models for diamond implemented in Allpix Squared.

Diamond is available as a material in Geant4 and can be used in Allpix Squared. The energy required to create electron–hole pairs and the Fano factor are taken from standard diamond detector literature [8]. The main missing components for a realistic detector-response simulation are diamond-specific mobility and trapping models, which we have implemented in this work.

2.1 Mobility models

Charge carrier transport in Allpix Squared is simulated using a drift–diffusion propagation model that accounts for charge carrier mobility in electric (and, where applicable, magnetic) fields, stochastic diffusion, and trapping. The drift velocity of charge carriers in a semiconductor under

an electric field \mathbf{E} is described by

$$\mathbf{v}_d(E) = \mu(E) \mathbf{E}, \quad (1)$$

where $\mu(E)$ is the field-dependent mobility. Diffusion is treated as a random walk process and linked to mobility via the Einstein relation,

$$D(E) = \frac{k_B T}{q} \mu(E), \quad (2)$$

with Boltzmann constant k_B , absolute temperature T and charge magnitude q . At each propagation step, the local electric field is evaluated and the carrier mobility is obtained from the selected parametrization. The corresponding drift velocity is then calculated and used to advance the carrier over the current step, such that the transport is governed by the instantaneous local conditions rather than by a single fixed mobility or velocity along the full trajectory.

Based on our recent review of charge-carrier mobility in diamond [4], we use the Piecewise mobility parametrization (PW model) to describe the drift of electrons. For holes we use the Caughey–Thomas (CT) model. The mobility model can be chosen and configured via the module configuration keys. For clarity, we show a minimal configuration example:

```
[TransientPropagation]
temperature = 300K
mobility_model = "diamond"
```

The model parameters used in this work [4] are summarized in [Table 1](#).

2.2 Trapping Model

Charge trapping reduces the collected signal and modifies the transient current response. For diamond detectors, trapping is conveniently characterized at detector level by the charge collection distance (CCD). For a planar sensor of thickness d , CCD relates to the charge collection efficiency (CCE) as

$$CCE \equiv \frac{Q}{Q_0} \approx \frac{CCD}{d}, \quad (3)$$

where Q_0 is the collected charge expected in the absence of trapping and Q is the collected charge in the presence of trapping.

To map CCD to an effective transport description, we use the Hecht relation [9] expressed in terms of effective carrier mean free paths (trapping lengths) λ_e and λ_h for electrons and holes, respectively,

$$\frac{Q}{Q_0} = \frac{\lambda_e}{d} \left(1 - e^{-d/\lambda_e}\right) + \frac{\lambda_h}{d} \left(1 - e^{-d/\lambda_h}\right). \quad (4)$$

This relation preserves the experimentally relevant mapping between CCD and collected charge. For unirradiated scCVD, trapping is usually negligible, and so $CCD \approx d$. In contrast, CCD is smaller than d for pcCVD due to intrinsic defects in particular at grain boundaries and in this case [Eq.4](#) implies that $CCD \approx \lambda$, where $\lambda = \lambda_e + \lambda_h$. In addition, radiation damage can lead to additional sources of trapping and so the CCD can be parameterized as

$$\frac{1}{CCD(\Phi)} = \frac{1}{CCD_0} + k \Phi, \quad (5)$$

Table 1: Parameters of the mobility models used for charge-carrier transport in Allpix Squared adopted from [4].

Carrier	Model	v_s (10^6 cm/s)	E_c (V/ μ m)	$\mu_{0,1}$ (cm^2/Vs)	$\mu_{0,2} = v_s/E_c$ (cm^2/Vs)	β (-)
Electrons	PW	26.59 ± 0.51	0.56 ± 0.00	1880 ± 4	4748 ± 92	0.41 ± 0.00
Holes	CT	15.09 ± 0.05	0.55 ± 0.00	-	2744 ± 9.4	0.88 ± 0.00

Note: Here, v_s is the saturation velocity, E_c the characteristic electric field, $\mu_{0,1}$ and $\mu_{0,2}$ the mobility scale parameters, and β the parameter controlling the transition towards velocity saturation.

where CCD_0 represents the unirradiated case ($\Phi = 0$) [10]. Within this effective description, the CCD of pcCVD diamond can be parameterized as a function of fluence and used as an input to simulate radiation-induced signal degradation. In the regime where charge collection is dominated by radiation damage or intrinsic defects, such as grain boundaries, the quantities CCD, effective trapping length (mean drift path), and fluence are thus related through an effective mapping:

$$\text{CCD} \leftrightarrow \lambda \leftrightarrow \Phi. \quad (6)$$

In this work, signal degradation caused by any agent (defects, grain boundaries, irradiation etc.) is evaluated outside the transport code and characterized by the CCD parameter.

Allpix Squared calculates the trapping probability as an exponential decay of the simulation time-step. As our description is in terms of CCD and mean drift path (λ), we calculate the trapping probability in terms of distance-step (Δx), so that for a drift distance Δx during a step, the probability to trap within that step is

$$P_{\text{trap}} = 1 - \exp\left(-\frac{\Delta x}{\lambda}\right). \quad (7)$$

Thus, trapping is integrated into stepwise propagation and affects the final charge carrier state as well as induced signals.

Mapping CCD to λ . The simulation accepts CCD as the primary detector-level trapping input, while Eq. 7 needs $\lambda = \lambda_e + \lambda_h$ as an input that we need to calculate from Eq. 4. Because it depends on λ_e and λ_h individually, we introduce a configurable ratio,

$$r \equiv \frac{\lambda_h}{\lambda_e}, \quad (8)$$

with default $r = 1.3$, adopted from [10] and with an option to override. For a given thickness d and an input CCD, we solve Eq. 4 for λ_e and then set $\lambda_h = r\lambda_e$.

The trapping model is selected by name and configured through sensor thickness, CCD, and the ratio r as follows:

```
[TransientPropagation]
trapping_model = "pcdiamond"
pcdiamond_thickness = 500um
pcdiamond_ccd = 260um
pcdiamond_lambda_ratio = 1.3
```

3 Experimental setups and measurements

This section summarizes the datasets and experimental setups used to validate the charge-transport simulations. For scCVD, we benchmark the simulated drift velocity and transient response against published reference measurements; the corresponding numerical data points were obtained by digitizing the values from the literature, details can be found in [11].

For pcCVD, we performed electrical (IV/CV), β -source CCD, and ^{241}Am -TCT measurements and compared the experimentally obtained data to the pcCVD simulation results. The pcCVD sensor used in this work is a planar diamond detector (Element Six) with an active area of $1 \times 1 \text{ cm}^2$ and a thickness of $d = 500 \mu\text{m}$.

We distinguish between unpumped and pumped pcCVD diamond detector states. ‘‘Pumping’’ (also referred to as priming) denotes a pre-irradiation of the diamond with ionizing radiation prior to data taking in order to fill trapping states and stabilize the internal field and electrical response, which typically improves the charge collection efficiency. In this work, pumping was performed by exposing the biased detector to a ^{90}Sr β source for ~ 20 min before applying the bias voltage and the corresponding measurement series.

3.1 Electrical Measurements

Electrical characterisation (IV/CV) is performed to define a stable bias range for subsequent CCD and TCT measurements. The current-voltage characteristics (IV curve) is measured to verify low leakage currents and the absence of early breakdown. This ensures that CCD (charge integration) and TCT pulse shapes are governed by bulk transport and trapping rather than contact artefacts or baseline drift. The measurements of capacitance-voltage profiles ensure electrostatic stability (approximately bias-independent capacitance), supporting the planar, near-uniform field assumption used to map V to E and to compare measured and simulated transients.

3.1.1 Current-voltage characteristics

Current-voltage characteristics were measured in steps of 20 V in a range from -1000 V to +1000 V for both unpumped and pumped states. For each voltage point, five readings were taken and the uncertainty is given by the standard deviation. Fig. 1 shows the leakage current as a function of the applied bias voltage for pumped (red) and unpumped (blue) sensors. The leakage current remained below ~ 0.4 nA over the full bias range. It increased only slightly and

approximately linearly with voltage, indicating stable, near-ohmic contact behaviour. Differences between pumped and unpumped IV curves were constant and about 0.1 nA.

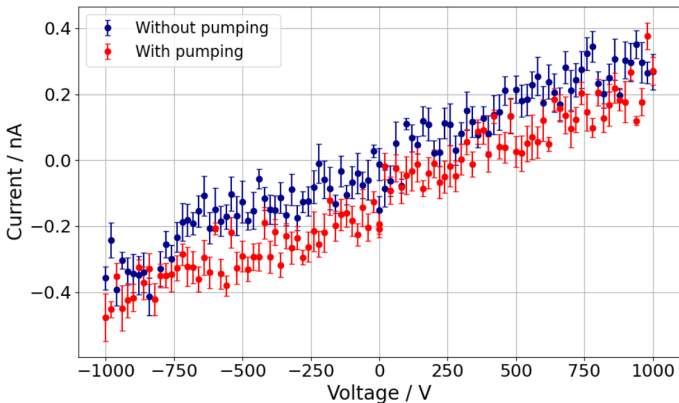


Figure 1: Leakage current as a function of applied bias. Data are shown without pumping (blue) and after 20 min pumping (red).

3.1.2 Capacitance-voltage profiles

Capacitance-voltage profiles were recorded over a range from -1000 V to $+1000$ V using a 20 kHz AC excitation with 0.5 V amplitude. As seen in Fig.2, the capacitance was essentially voltage-independent at approximately 6.127 pF. After pumping it decreased slightly but remained stable. The first bias point shows a small deviation from the otherwise flat plateau, which is compatible with a settling artefact (HV/instrument stabilization and cable/fixture charging) immediately after the initial high-voltage step. A parallel-plate estimate using $\epsilon_r \approx 5.7$, $A = 1$ cm² and $d = 500$ μ m yields about 10.09 pF, i.e. higher than the measured value, suggesting additional geometric/electrode/fixture effects beyond the simplified model.

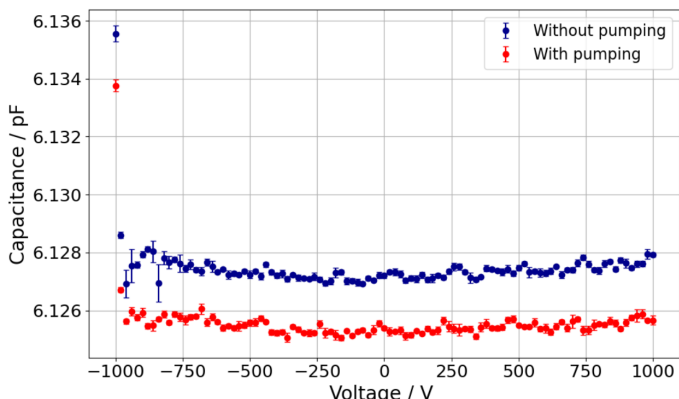


Figure 2: Detector capacitance as a function of applied bias. Data are shown before pumping (blue) and after 20 min pumping (red).

3.2 CCD/CCE measurements

3.2.1 Experimental setup and readout chain

The detector was operated in a coincidence setup with a ⁹⁰Sr β source (sealed source, activity $A = 37$ MBq on 20.11.1995). The source is in secular equilibrium with its daughter ⁹⁰Y and therefore emits a continuous β^- spectrum with endpoint energies of $E_{\max} = 0.546$ MeV (⁹⁰Sr \rightarrow ⁹⁰Y)

and $E_{\max} = 2.28$ MeV (⁹⁰Y \rightarrow ⁹⁰Zr). The source was placed above the diamond, while a plastic scintillator located downstream (below the diamond) served as an event trigger for traversing particles. The scintillator output was digitized as the trigger reference, and the diamond signal was processed by a spectroscopic shaping amplifier before digitization.

The diamond was read out using an ultra-low-noise, inverting CIVIDEC Cx-L Spectroscopic Amplifier [12], with an integrated shaping stage producing a Gaussian output pulse with ~ 180 ns FWHM, a gain of 12.5 mV/fC, and an integrated Bias-Tee (HV input) for detector biasing. The amplifier is specified with an equivalent noise charge of $(300 + 10/\text{pF})$ electrons, and provides a linear output range of ± 2 V with a linear input range of 180 fC. An ISEG SHQ 222M high voltage power supply was used for the scintillator trigger (-1000 V), an ISEG SHR Precision DC high-voltage power supply was used for the biasing of the diamond detector, and a TENMA 72-2710 power supply was used for the amplifier.

3.2.2 Data acquisition

Waveforms were acquired with a Tektronix MSO5204B oscilloscope (2GHz, 10GS/s), controlled remotely via VISA/TCP-IP [13]. The Cx amplifier output was connected to oscilloscope channel 1 (CH1) and the scintillator trigger to channel 2 (CH2). Both channels were operated with 50 Ω input termination.

The oscilloscope was configured for triggered waveform acquisition with Record length $N_{\text{samples}} = 1000$ points per waveform and 2000 triggered waveforms were stored per bias setting.

3.2.3 Offline pulse-height (charge) reconstruction

Each stored waveform $V(t)$ is reduced to one charge estimator per event.

Baseline subtraction and noise estimation are performed in a baseline-only interval. The baseline level b and the baseline noise σ_{base} are estimated robustly from the samples in the baseline interval using the median and the median absolute deviation ($\text{MAD}_i = \text{median}(|V_i - b_i|)$),

$$b_i = \text{median}(V_i), \quad \sigma_{i(\text{base})} = 1.4826 \times \text{MAD}_i, \quad (9)$$

evaluated over the baseline interval. The factor 1.4826 makes the MAD a consistent estimator of the standard deviation for Gaussian noise (since $\text{MAD} = 0.6745\sigma$ for a Gaussian distribution). A polarity factor $p = \pm 1$ is applied such that the expected diamond pulse polarity is mapped to a positive excursion:

$$y_{\text{eff}}(t) = p(V(t) - b). \quad (10)$$

The signal peak amplitude A_{sig} is defined as the maximum of $y_{\text{eff}}(t)$ within a coincidence (signal) window aligned to the scintillator-trigger timing. A noise-peak estimator A_{noise} is analogously defined as the maximum of $y_{\text{eff}}(t)$ in a baseline-only window centered.

3.2.4 Event selection (cuts)

Events are accepted if they satisfy all of the following quality criteria:

1. **SNR:** $A_{\text{sig}}/\sigma > \text{SNR}_{\text{cut}}$, with default $\text{SNR}_{\text{cut}} = 3$.
2. **Coincidence-time:** the signal peak time t_{peak} must lie inside the coincidence window.
3. **Dominance:** the peak of the windowed signal must coincide with the global maximum of $y_{\text{eff}}(t)$ within a tight tolerance (10^{-3} relative), rejecting events where the largest amplitude is outside the coincidence window.

For each bias setting, the number of events passing the waveform-quality criteria was recorded. Bias points with fewer than 1700 accepted events were excluded to ensure sufficient statistics for a stable pulse-height spectrum. The corresponding CCD dataset is available in the TUDODATA research data repository [14].

3.2.5 Charge calibration, MPV extraction, and CCD

The pulse-height is converted into an input charge using the amplifier gain G ,

$$Q [\text{fC}] = \frac{A_{\text{sig}}[\text{M}] [\text{mV}]}{G [\text{mV}/\text{fC}]}. \quad (11)$$

Fig. 3 shows the charge spectrum of the accepted events, fitted with a Landau distribution convoluted with a Gaussian response function (Langau model). The most-probable value (MPV) of the fitted spectrum, Q_{MPV} , is used to estimate the collected charge.

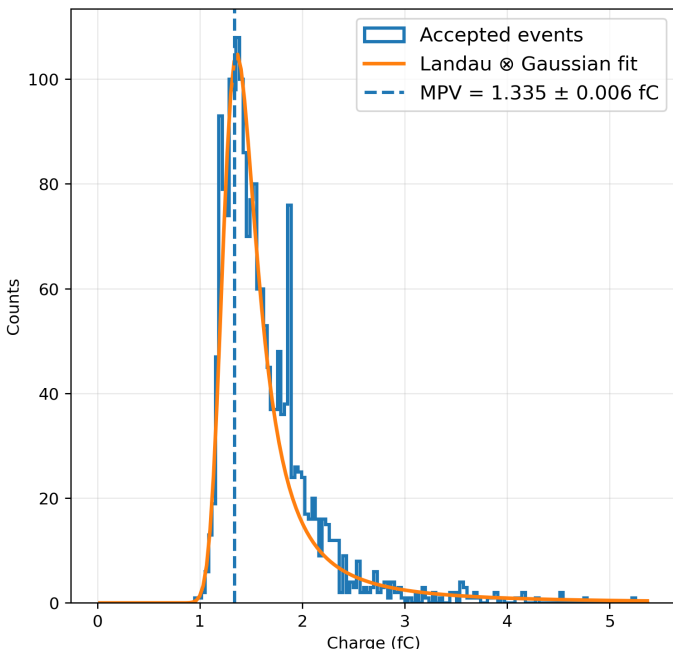


Figure 3: Landau + Gaussian distribution (using Sr-90) at an electric field of $0.4 \text{ V}/\mu\text{m}$ fitted with langau model to events accepted by the three selection criteria mentioned in Sec. 3.2.4.

The CCD is computed from Q_{MPV} by converting femto-coulomb to electrons and dividing by the assumed electron-hole yield n_{eh} per micrometer (default $n_{\text{eh}} = 36$ pairs/ μm),

$$\text{CCD} [\mu\text{m}] = Q_{\text{MPV}} [\text{fC}] \times \frac{6241.5}{n_{\text{eh}}}. \quad (12)$$

Here, 6241.5 is the conversion factor from femto-coulomb to elementary charges i.e. $1 \text{ fC} \approx 6241.5$ electrons.

The uncertainties reported for CCD are statistical and derived from the Langau fit uncertainty on the MPV,

$$\delta\text{CCD} = \delta Q_{\text{MPV}} \times \frac{6241.5}{n_{\text{eh}}}, \quad \delta\text{CCE} = \frac{\delta\text{CCD}}{d}. \quad (13)$$

Systematic uncertainties (e.g. gain calibration, assumed n_{eh} , thickness tolerance, and residual baseline systematics) are not included.

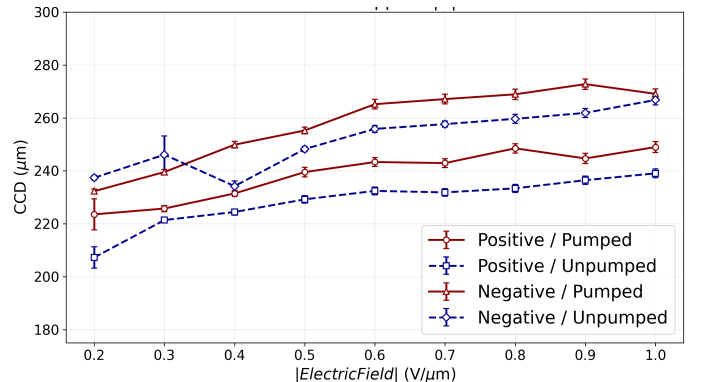


Figure 4: CCD of pcCVD diamond, extracted from ^{90}Sr spectra as a function of $|E| = |V|/d$. Results are shown for both bias polarities in the unpumped state (blue) and after ~ 20 min β -pumping (red). Error bars denote the statistical uncertainty of the MPV from the Landau-Gaussian (Langau) fit.

Fig. 4 shows the charge collection distance (CCD) extracted from the ^{90}Sr spectra as a function of the absolute electric field $|E| = |V|/d$ for the two bias polarities, each measured in the unpumped state and after ~ 20 min of β -pumping. For all configurations, the CCD increases with $|E|$ from $\sim (205\text{--}235) \mu\text{m}$ at $|E| = 0.2 \text{ V}/\mu\text{m}$ to a quasi-saturation regime above $|E| \gtrsim 0.6 \text{ V}/\mu\text{m}$, indicating reduced effective trapping at higher electric fields. Pumping improves charge collection which is consistent with trap filling and/or partial depolarization of the bulk. A clear polarity dependence is observed over the full field range. Since the coincidence requirement selects β particles that traverse the sensor and reach the downstream scintillator, electron-hole pairs are generated throughout the full detector thickness for both bias polarities. The observed polarity dependence therefore most likely reflects asymmetric charge transport and collection, e.g. a non-uniform distribution of trapping centers and/or carrier-dependent trapping. In our pcCVD sample, the irradiated backside corresponds to the growth side, where grain boundaries and related defects are expected to be more abundant. Reversing the bias swaps which carrier species drifts towards this region. For negative bias, electrons drift towards the growth side, whereas for positive bias, holes drift towards it. If hole trapping is stronger near the growth side, this naturally leads to a reduced CCE/CCD for positive bias, consistent with the measured asymmetry.

The negative-bias configuration yields a higher CCD than the positive-bias configuration by typically $\sim (15\text{--}30) \mu\text{m}$, corresponding to a relative CCE difference of a few percent for a $500 \mu\text{m}$ thick sensor.

3.3 Transient Current Measurements

Transient Current Technique (TCT) measurements were performed to study the time-domain response of the diamond sensor under localized charge injection and to extract pulse-shape and timing characteristics (rise/fall times, pulse widths), which are directly dependent on the internal electric field, carrier drift, and polarization/trapping. In contrast to the β -source CCD measurements in Sec. 3.2, TCT uses a localized energy depositing source and records the full current transient waveform for each event and charge carrier type.

3.3.1 Experimental setup and readout chain

The same diamond detector (as in Sec. 3.2) was irradiated with an ^{241}Am α source (activity $A = 5$ kBq on 28.03.1996). The detector was illuminated from the back side (grounded electrode), while the front side was connected to the HV supply and read out via a broadband TCT amplifier. This geometry ensures that the charge deposition occurs close to the grounded electrode. Depending on the chosen field direction, one carrier species traverses most of the sensor thickness while the other is collected close to the generation side, enabling carrier-sensitive pulse-shape studies.

The readout used a CIVIDEC C2-TCT broadband current amplifier [15] with integrated Bias-Tee for simultaneous biasing and signal extraction. The amplifier provides 40 dB gain, a bandwidth of 0.01–2 GHz, and is optimized for TCT transients from the ns range up to 50 μs . The amplifier output was digitized by a Tektronix MSO5204B oscilloscope.

3.3.2 Data Acquisition

Waveforms were acquired with a Tektronix MSO5204B oscilloscope controlled remotely via VISA/TCP-IP using a dedicated Python acquisition script, with 50 Ω termination. The trigger levels (± 14 mV (unpumped), ± 18 mV (pumped)), record length (1000), sampling rate (10 GS/s), and number of repetitions (2000) were set via an external configuration file read by the acquisition script. For each triggered event, the full raw waveform $V(t)$ was stored.

3.3.3 Event selection

Offline processing and selection were performed by estimating a baseline level b_i and baseline noise σ_i , for each waveform, in a baseline-only interval using robust estimators (Eq.9). The waveform is baseline-subtracted and automatically sign-flipped such that the transient pulse is positive,

$$V_i^{\text{corr}}(t) = p(V_i(t) - b_i), \quad p = \pm 1, \quad (14)$$

where p is chosen from the population statistics of the individual waveform polarities.

A signal window $t \in [9 \text{ ns}, 17 \text{ ns}]$, a baseline window ending at 4 ns, and a noise-charge window $([0 \text{ ns}, 8 \text{ ns}]$ were defined with automatic relocation to avoid overlap with the signal window. An optional late-time “ringing” window (default $[20 \text{ ns}, 25 \text{ ns}]$) can be used to quantify pickup/ringing.

For each event, the script defines a positive-only integrated

charge in the signal window,

$$Q_i^{\text{sig}} = \int_{\text{sig}} \max(V_i^{\text{corr}}(t), 0) dt, \quad (15)$$

and an analogous quantity Q_i^{noise} in the noise window. The noise scale σ_Q is estimated robustly from the Q^{noise} distribution (MAD), and the primary selection metric is

$$\text{SNR}_Q = \frac{Q_i^{\text{sig}} - \text{median}(Q^{\text{noise}})}{\sigma_Q}. \quad (16)$$

The default requirement is $\text{SNR}_Q > 3$. Events are accepted based on a combination of (i) the SNR_Q requirement, (ii) a dominance cut requiring that the maximum excursion in an early-time search region coincides with the signal-window peak (suppressing late ringing), and (iii) basic finiteness/positivity checks so that waveforms are rejected if the extracted parameters are numerically broken or have impossible sign/value.

Additional cuts include an amplitude-based SNR (A_{sig}/σ_i , where $A_{\text{sig}} = \max V_i^{\text{corr}}(t)$), a template correlation coefficient ρ , an effective-width outlier rejection using $R_{\text{eff}} = Q_i^{\text{sig}}/A_{\text{sig}}$, and an optional ringing metric based on the late-time RMS relative to baseline noise.

For visualization and mean-waveform stability, narrowband pickup sinusoids were subtracted using only pulse-free regions (baseline + late tail). This is performed after the event selection and therefore does not change the acceptance.

3.3.4 Mean waveform and Transient Times

Timing observables are extracted from the mean waveform of the accepted event set,

$$\bar{V}(t) = \frac{1}{N} \sum_{i \in \text{good}} V_i^{\text{corr}}(t), \quad (17)$$

and both the event-to-event standard deviation band and the standard error of the mean (SEM) are produced for diagnostics. Several parameters are extracted from \bar{V} : (i) peak time t_{peak} and amplitude A_{peak} (peak constrained to the signal window), (ii) FWHM from the 50% level crossings, (iii) rise time $t_{90} - t_{10}$ and fall time $t_{10} - t_{90}$ from 10% and 90% crossings, and (iv) an edge-defined pulse width using a configurable edge threshold

$$V_{\text{edge}} = \max(f_{\text{edge}} A_{\text{peak}}, k_{\sigma} \sigma_{\text{base}}), \quad (18)$$

where f_{edge} and k_{σ} are user parameters (defaults: $f_{\text{edge}} = 0.10$, $k_{\sigma} = 0$).

For the accepted digitized waveforms, an additional pulse-width observable is derived from the analytic-signal envelope. For the mean waveform $x[n]$, the discrete analytic signal is constructed using an FFT-based Hilbert transform, and the envelope is defined as $a[n] = |z[n]|$. The corresponding envelope FWHM is then obtained as the time interval between the rising and falling half-maximum crossings of $a[n]$, determined by linear interpolation between adjacent samples. Compared with the direct waveform FWHM, this observable is less sensitive to small oscillatory structures in the transient. The extracted transient signals and the corresponding timing observables are shown in Fig.5.

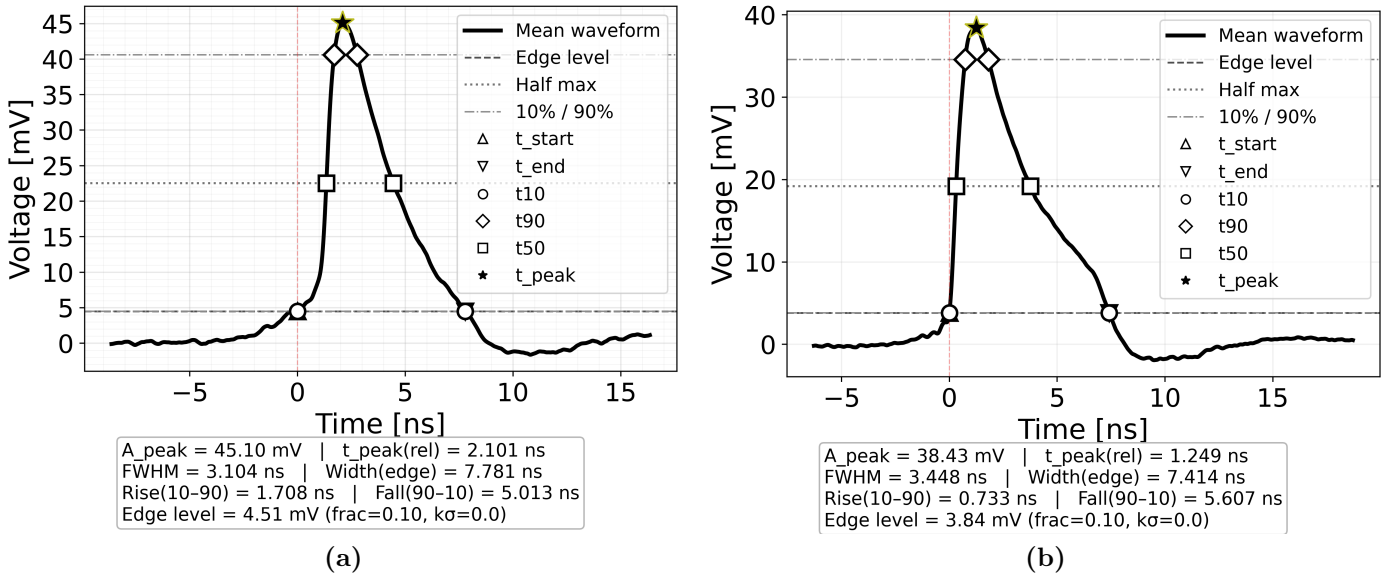


Figure 5: Mean measured transient current waveforms at $E = 1 \text{ V}/\mu\text{m}$ for (a) electrons and (b) holes. The markers indicate the characteristic timing points used in the waveform analysis, namely the 10%, 50%, and 90% level crossings on the leading and trailing edges, together with the peak position. The corresponding values of the peak amplitude, rise time, fall time, full width at half maximum (FWHM), and edge-defined pulse width are reported in each panel.

The same envelope-FWHM procedure is also applied on an event-by-event basis for accepted events only and retained as a quality-control observable. For each bias setting, the analysis produces a compact set of summary and diagnostic output files.

Relation to Ramo–Shockley theorem and weighting field. The measured TCT transient is interpreted in terms of the induced current on the readout electrode via the Ramo–Shockley theorem. For a moving charge q with drift velocity $\mathbf{v}(t)$, the instantaneous induced current is

$$i(t) = q \mathbf{v}(t) \cdot \mathbf{E}_w(\mathbf{x}(t)), \quad (19)$$

where \mathbf{E}_w is the *weighting field* obtained by setting the readout electrode to unit potential, all other electrodes to zero, and neglecting space charge (pure electrostatics). For an ideal planar pad geometry, \mathbf{E}_w is approximately uniform with magnitude $|\mathbf{E}_w| \simeq 1/d$, such that the current waveform is directly proportional to the carrier drift velocity (and thus to the local electric field through $\mathbf{v} = \mu\mathbf{E}$ in the non-saturated regime). The time integral of the transient yields the induced charge,

$$Q_{\text{ind}} = \int i(t) dt = q \Delta\phi_w, \quad (20)$$

where $\Delta\phi_w$ is the change in weighting potential along the carrier trajectory; in the ideal planar case, carriers traversing the full thickness contribute approximately q to the integral. Deviations of the pulse shape from the ideal rectangular/triangular forms—as well as polarity/illumination-side dependencies—therefore reflect non-uniform internal fields (e.g. polarization), carrier trapping/detrapping, and velocity saturation, and provide a direct basis for comparison to simulated transients computed from the same $E(\mathbf{x})$ and weighting-field model.

4 Simulations and Results

We have simulated charge-carrier drift in diamond using a single-pixel geometry in Allpix Squared by defining a diamond sensor with variable dimensions (default: $4 \times 4 \times 0.5 \text{ mm}^3$), as shown in Fig. 6. No explicit contacts were defined. An ^{241}Am α point source was placed $1 \mu\text{m}$ above the top surface of the diamond.

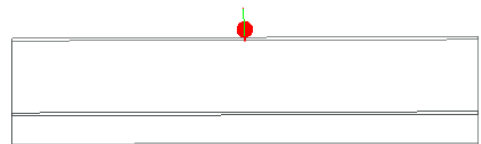


Figure 6: Schematic of the simulated diamond sensor geometry, indicating the sensor thickness and the position of the Am-241 source. The red marker denotes the source location.

To verify that the simulated charge-carrier polarity assignment (electrons or holes) is consistent with the chosen simulation setup, we examined the transport profiles at $E = 0.18 \text{ V}/\mu\text{m}$, shown in Fig. 7. As expected for scCVD with $\lambda \geq \text{CCD}$, the drift (forward spread) dominates the diffusion (lateral spread) and full charge is collected. The Alpha particle emitted by Am-241, deposits all its energy in the first $10 \mu\text{m}$ of the sensor thickness, hence only one kind of charge carrier traverse the full thickness of the sensor.

4.1 scCVD mobility validation

We validated the scCVD drift velocity and transient response against published reference measurements [4,7,11].

4.1.1 Electrons (PW model)

The PW model was validated in two different ways, namely the time of arrival and the transient pulses. The two approaches complement each other and both support the validity of the model.

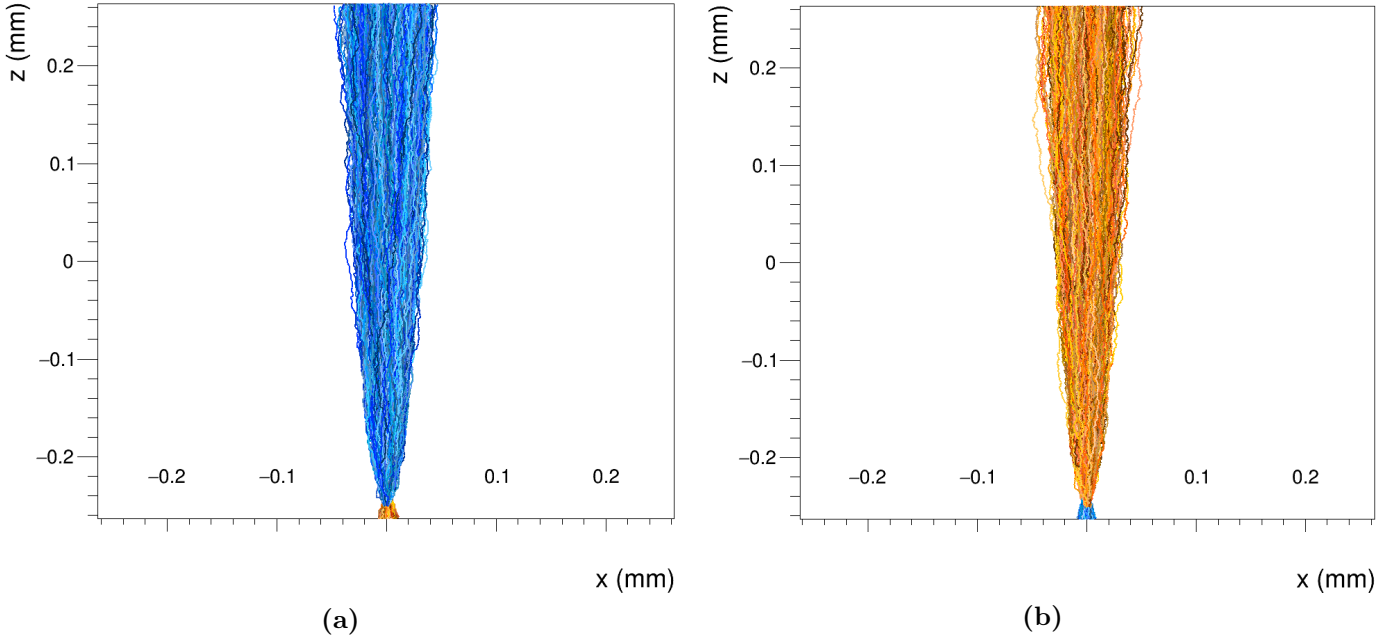


Figure 7: Representative simulated charge-carrier transport trajectories of (a) electrons and (b) holes at $E = 0.18 \text{ V}/\mu\text{m}$. The plots show the projected transport paths and their lateral spread during drift through the sensor bulk. The incident Am-241 (bottom) deposits all its energy within few micrometers of the sensor. The horizontal axis is not to scale and does not correspond to the physical lateral dimension of the sensor.

Time of arrival. Using the `GenericPropagation` module, charge-carrier drift was simulated for 60 bias-voltage values ranging from -1 V to -40000 V . For this polarity of the bias voltage, only electrons traversed the full thickness of the diamond. For a sensor thickness d and an extracted drift time (time of arrival) $t(E)$, the drift velocity was calculated as

$$v_d(E) = \frac{d}{t(E)}. \quad (21)$$

Fig.8(a) shows the extracted $v_d(E)$ from the simulation together with digitized literature data. Relative residuals are also shown to quantify the agreement. The simulated results agree well with the literature data.

Transient pulses and transient time. Using the `TransientPropagation` module, charge-carrier drift was simulated and transient pulses were extracted from the simulation output for different electric fields. The transient time was estimated from the full width at half maximum (FWHM) of the corresponding pulses, as shown in Fig.9(a). The drift velocity was then calculated for the respective electric fields using Eq.21. Fig.8(a) shows the resulting $v_d(E)$ dependence obtained from the transient-pulse simulations together with digitized literature data. Relative residuals are included to quantify the level of agreement. Overall, the simulated drift velocities are consistent with the literature data within the investigated field range.

The simulated transient pulse was subsequently processed with an amplifier model using a gain of 53 dB and a bandwidth of $0.01\text{--}2 \text{ GHz}$, consistent with the characteristics reported in Ref.[16], and employed in the measurements of Ref.[7]. The amplified simulated transients were then compared with experimentally measured transient pulses from a $526 \mu\text{m}$ -thick scCVD diamond sample, as shown in Fig.10(a). The simulated transients exhibit a steep rise within the first nanosecond, followed by an approximately

constant plateau and a rapid fall-off at the end of the signal. The experimentally reported transient pulses show broader rising and falling edges, reflecting the finite temporal response of the experimental setup, which is not fully included in the simulation. Overall, the simulations reproduce the main features of the measured waveforms and capture the observed pulse evolution. The signals shown correspond to an electric field of $0.18 \text{ V}/\mu\text{m}$.

4.1.2 Holes (CT model)

The implementation of the CT model for holes was validated by following the same approaches described in Sec.4.1.1. The corresponding simulation results are shown in Fig.8(b), Fig.9(b), and Fig.10(b), and they are in good agreement with the experimentally measured data.

4.2 pcCVD CCD/trapping validation

We have validated the implementation of the trapping model to reproduce measured TCT pulse shapes by comparing simulated transients with laboratory waveforms obtained using an Am-241 source (see Sec.3.3). In this validation, the experimentally determined CCD values (at $E = 1 \text{ V}/\mu\text{m}$) from Fig.4 were used as inputs to the trapping model. The simulated transients were subsequently processed with the same signal-treatment procedure adopted for the experimental analysis, including the effective gain corresponding to the CIVIDEC TCT readout chain [15], such that the comparison is performed at the level of the reconstructed waveform observables.

Fig.11 shows the resulting comparison at $E = 1 \text{ V}/\mu\text{m}$ for electron and hole drift. In both cases, the simulation reproduces the principal pulse amplitude scale, the time of the maximum, and the overall signal duration.

For the electron signal, the simulated waveform shown in

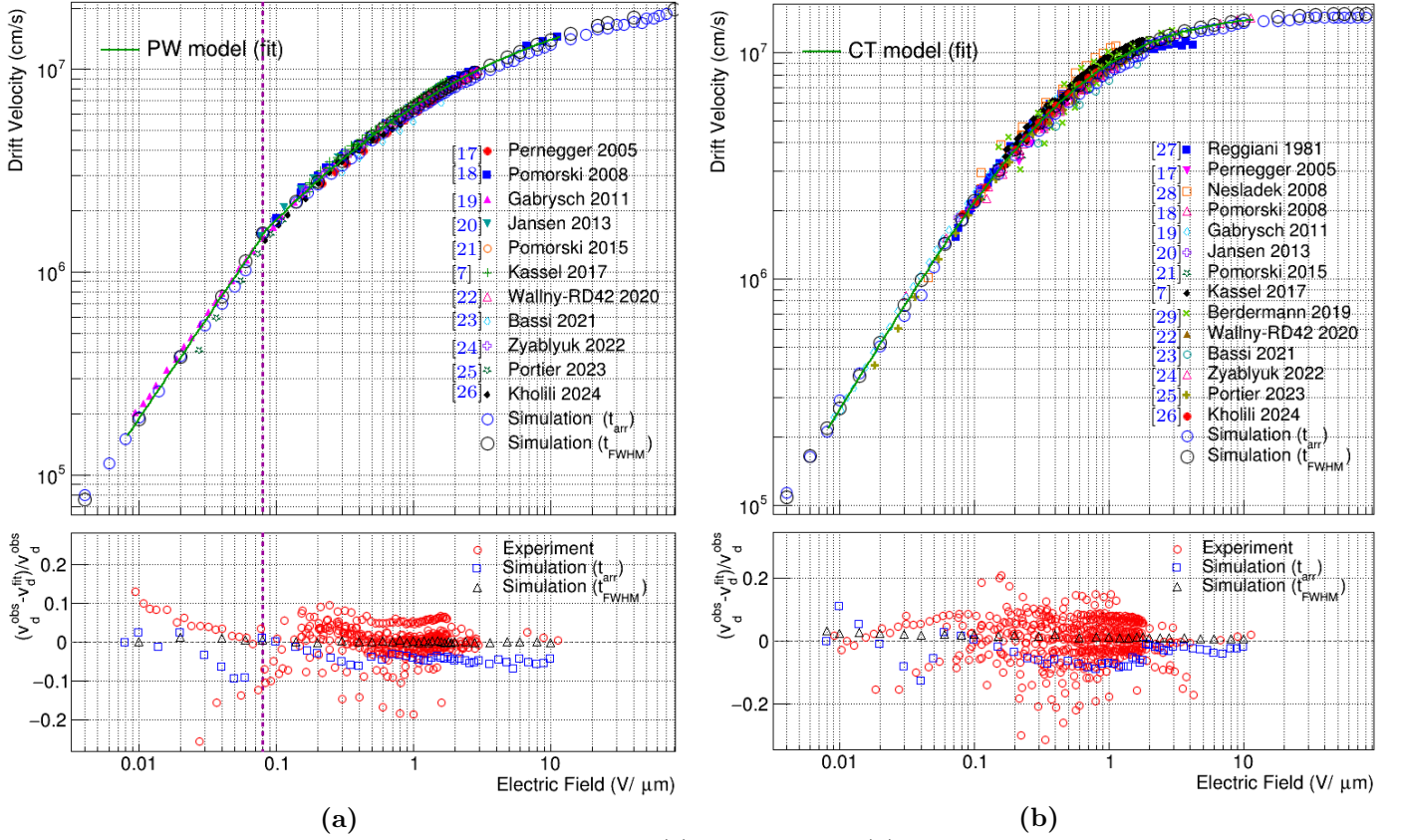


Figure 8: Drift velocity as a function of electric field for (a) electrons and (b) holes, comparing simulation results with experimental data. The green line shows the fitted model obtained from the experimental data and corresponding to the parameterization used in the simulation. It is included to facilitate comparison of the simulation results with the model prediction. The lower panels show the relative residuals, $(v_d^{\text{obs}} - v_d^{\text{fit}})/v_d^{\text{obs}}$, as a function of E , highlighting the agreement between the simulation and the data used to parameterize the models implemented in the simulation framework. The scatter in the “Simulation (t_{arr})” points reflects the uncertainty in the determination of the mean time of arrival.

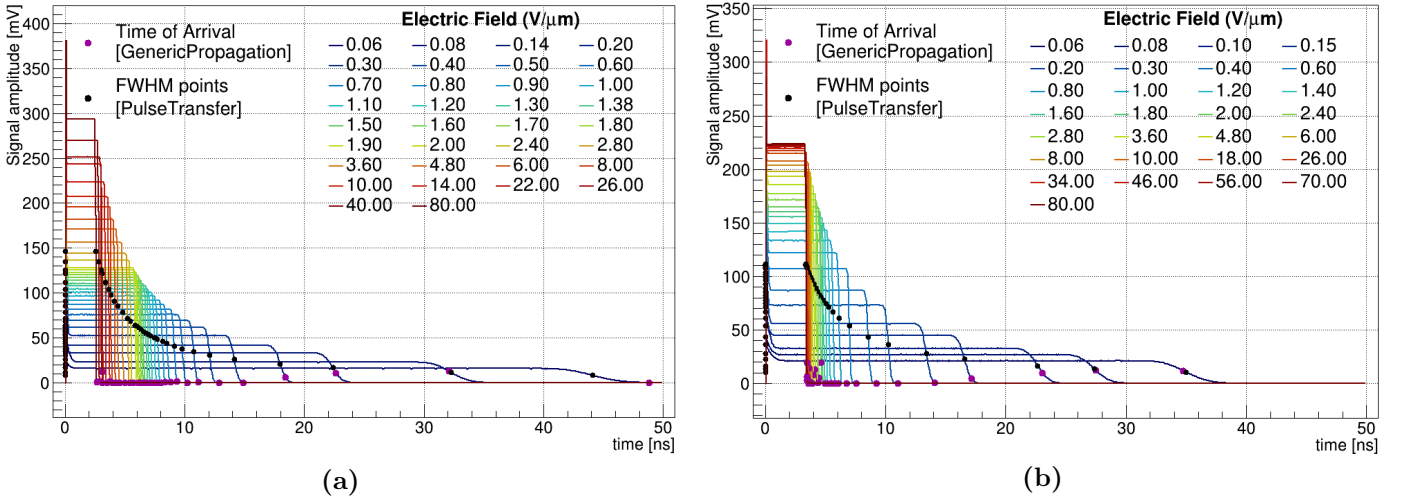


Figure 9: Simulated transient current waveforms (at given electric fields) used for the extraction of transit times for (a) electrons and (b) holes. The black markers indicate the $t_{50\%}$ values on the leading and trailing edges, from which the FWHM is determined. The magenta markers represent the time-of-arrival values obtained from `GenericPropagation`.

Fig.11(a) is post-processed prior to comparison with the measured signals. In particular, the simulated transients are filtered to account for the finite bandwidth of the readout chain, and an additional smoothing/superposition procedure is applied in order to approximate the experimentally observed signal shape. The post-processed simulation remains characterized by a steeper leading edge than observed in the measured mean waveform, indicating that the initial rise of the induced signal is still not fully reproduced. In

contrast, the agreement on the trailing edge is significantly better. The simulated decay follows the measured waveform over most of the falling part of the pulse, including the slower decrease at low amplitudes. A residual difference is visible in the late-time structure, where the simulated waveform exhibits a cusp-like feature below the 10% level that is not clearly resolved in the experimental waveform.

For the hole signal in Fig.11(b), the agreement between sim-

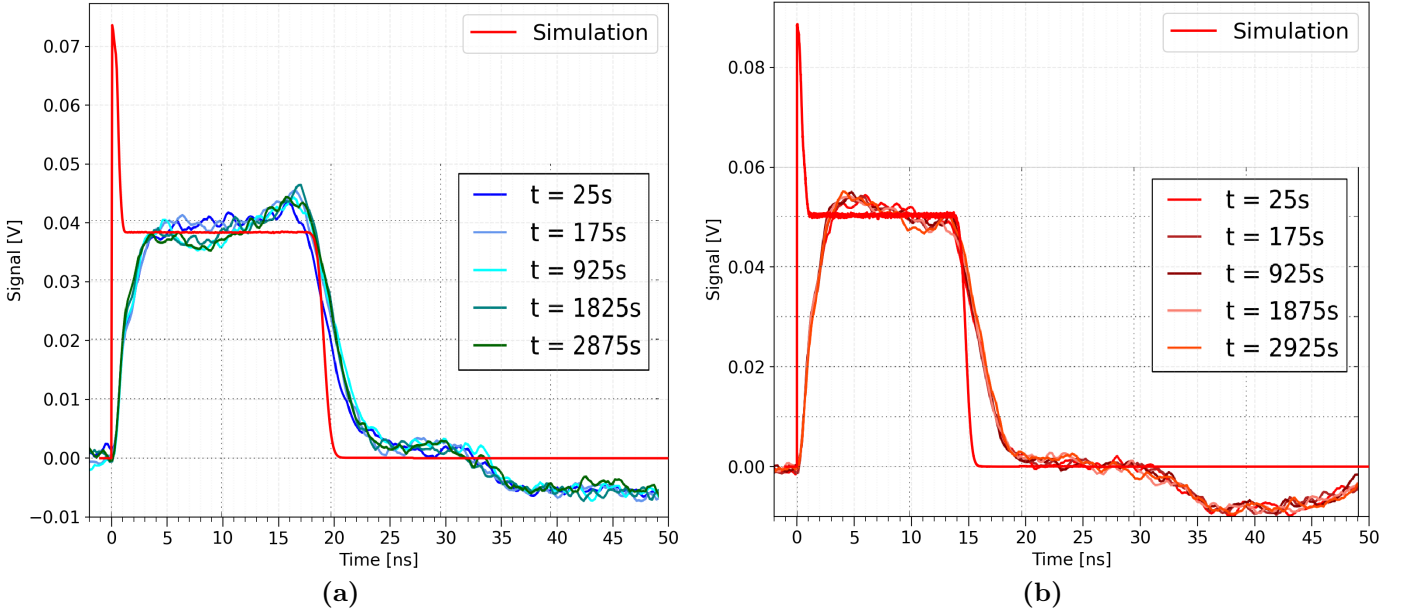


Figure 10: Comparison of simulated (red) and experimentally measured TCT signals in scCVD diamond at $E = 0.18 \text{ V}/\mu\text{m}$ for (a) electrons and (b) holes, using the experimental data from Ref. [7]. The color scale represents the evolution of the measured signal shape with polarization time. Polarization effects are not implemented in the present work.

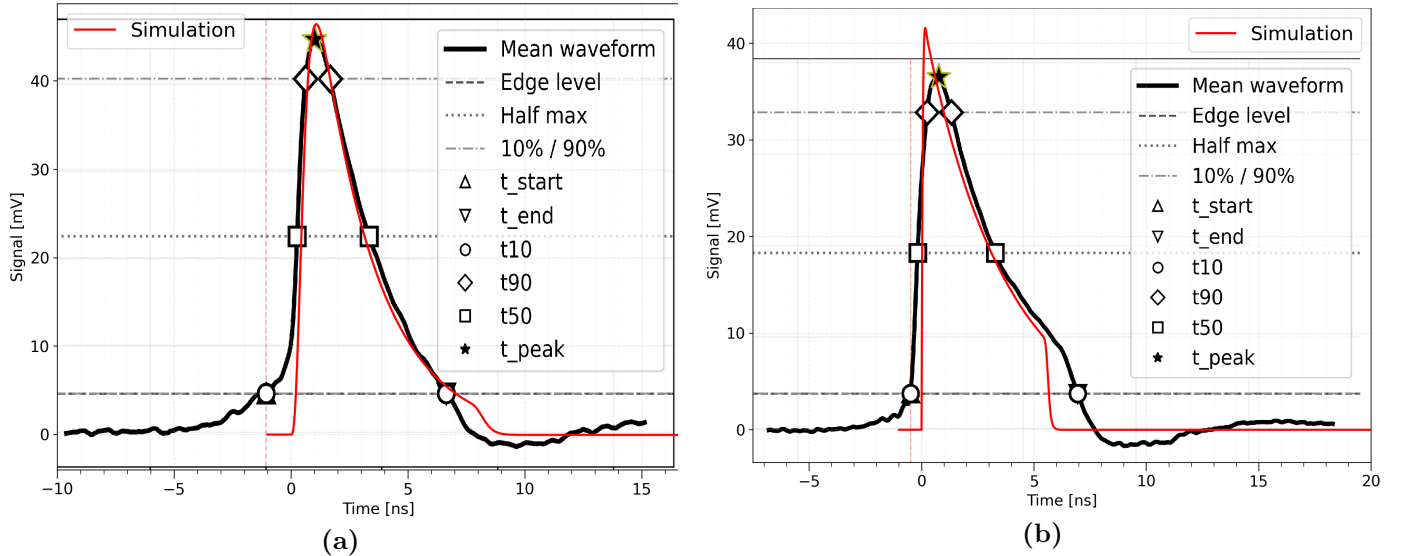


Figure 11: Comparison of simulated (red) and experimentally measured (colored) TCT waveforms in pcCVD diamond at $E = 1 \text{ V}/\mu\text{m}$ for (a) electrons and (b) holes. The red curves represent the post-processed simulation output and the black curves the mean measured waveforms. The indicated timing markers are derived from the measured signal and illustrate the leading-edge development, peak position, and trailing-edge evolution used for the waveform comparison.

ulation and measurement is generally satisfactory, with the pulse duration reproduced to reasonable accuracy. In this case, the post-processing applied to the simulated waveform consists only of amplification by the effective gain of the readout chain, $G = 43 \text{ dB}$. The most visible discrepancy is located on the leading edge, where the simulated signal rises more abruptly than the measured waveform due to the absence of additional frequency-domain convolution and reaches a slightly higher maximum at an earlier time. In contrast, the trailing-edge evolution is reproduced more accurately, indicating that the effective trapping description captures the dominant charge-loss behaviour during the decay of the pulse. Smaller differences remain in the late-time baseline recovery. These residual deviations are consistent with the use of an effective trapping parameterization based on CCD input data, which reproduces the

integral charge-loss behaviour but does not explicitly resolve the microscopic distribution of trapping centres, local electric-field distortions, or grain-dependent transport paths in the material.

Overall, the waveform comparison demonstrates that the implemented pcCVD model reproduces the dominant features of the measured TCT response at the field considered here. The remaining discrepancies are localized primarily in the leading-edge development and in the late trailing-edge structure, indicating that the current implementation captures the first-order transport behaviour while second-order effects associated with detector-response convolution and material inhomogeneity remain outside the present description.

5 Conclusions and outlook

We have extended Allpix Squared with diamond-specific charge-transport models by implementing field-dependent mobility parameterizations for electrons and holes, together with an effective trapping description based on the charge collection distance (CCD). This provides a practical detector-level framework for simulating charge transport, transient signals, and charge collection in both scCVD and pcCVD diamond sensors.

For scCVD diamond, the mobility implementation was validated against published reference data using three complementary approaches. Drift velocity extracted from time-of-arrival simulations, drift velocity derived from transient times, and direct comparison of simulated and measured TCT waveforms. These mutually reinforcing validation paths show that the implemented transport models reproduce the measured carrier dynamics with good consistency over the investigated electric-field range.

For pcCVD diamond, we demonstrated that the CCD-based trapping interface reproduces the reduced charge collection and degraded transient signal shapes observed experimentally. By using measured CCD values as external inputs, the model provides a simple and experimentally accessible way to incorporate effective trapping into detector-response simulations. In this form, the implementation establishes a useful link between laboratory characterization and end-to-end detector simulation.

The present approach is intended as an effective detector model rather than a microscopic description of defect physics. Its main strength is therefore its applicability to practical studies of signal formation, timing performance, and charge collection in diamond detectors under different operating conditions and material qualities.

Future work will focus on extending the model beyond the present effective CCD description. In particular, the inclusion of polarization effects, non-uniform internal electric fields, and spatially varying trapping in pcCVD material would further improve the realism of the simulation. Additional validation against a broader range of detector thicknesses, bias conditions, and irradiation-dependent CCD parameterizations will also be important to define the predictive range of the model for radiation-damage studies and detector optimization.

Acknowledgments/Funding: This work was supported by the Alexander von Humboldt Foundation.

The authors acknowledge the use of the wafer prober at TU Dortmund, funded by the Deutsche Forschungsgemeinschaft (DFG, German Research Foundation) under grant number 450639102.

The authors further thank **Dustin Dobrinsky** for developing the CCD data-acquisition script, and **Simon Spannagel** and **Paul Schütze** for valuable discussions and comments on developing the simulation chain.

CRedit authorship contribution statement: **Faiz Rahman Ishaqzai:** Conceptualization, Methodology, Investigation, Data curation, Formal analysis, Writing – orig-

inal draft, Visualization. **Muhammed Deniz:** Supervision, Writing – review & editing, Visualization. **Kevin Kröninger:** Funding acquisition, Supervision, Validation, Writing – review & editing, Visualization. **Marta Baselga** Methodology, Data Curation. **Tobias Bisanz** Software. **Jens Weingarten:** Conceptualization, Supervision, Validation, Writing – review & editing. **Antonia Wippermann:** Investigation, Data curation, Formal analysis of IV/CV measurements, Investigation (TCT data acquisition).

Declaration of competing interest: The authors declare that they have no known competing financial interests or personal relationships that could have appeared to influence the work reported in this paper.

Data availability: The electron and hole drift-velocity and mobility data (literature) used in this study are available in the TUDOData research data repository of TU Dortmund University at [doi:10.17877/TUDODATA-2025-MIESBVS](https://doi.org/10.17877/TUDODATA-2025-MIESBVS).

The CCD data taken with scintillator trigger setup is available at doi.org/10.17877/TUDODATA-2026-ODJ7MD. The Electrical measurement and TCT data is available at reasonable request at the moment, and will be deposited to the TUDOData research data repository.

Declaration of generative AI and AI-assisted technologies in the manuscript preparation process: During the preparation of this work the authors used AI in order to improve wording and sentence structure. After using these tools, the authors reviewed and edited the content as needed and take full responsibility for the content of the publication.

References

- [1] AJ Edwards et al. “Radiation monitoring with diamond sensors in BABAR”. In: *IEEE Transactions on Nuclear Science* 51.4 (2004), pp. 1808–1811.
- [2] A. J. Edwards et al. “Radiation monitoring with CVD diamonds in BABAR”. In: vol. 552. IEEE, Oct. 2005, pp. 176–182. DOI: [10.1016/j.nima.2005.06.028](https://doi.org/10.1016/j.nima.2005.06.028).
- [3] B. Aubert et al. “The BaBar detector: Upgrades, operation and performance”. In: *Nuclear Instruments and Methods in Physics Research Section A: Accelerators, Spectrometers, Detectors and Associated Equipment* 729 (2013), pp. 615–701. ISSN: 0168-9002. DOI: <https://doi.org/10.1016/j.nima.2013.05.107>.
- [4] Faiz Rahman Ishaqzai et al. *Charge-Carrier Mobility in Diamond: Review, Data Compilation, and Modelling for Detector Simulations*. Revised manuscript under review at *Diamond and Related Materials*. 2026. arXiv: [2601.10807](https://arxiv.org/abs/2601.10807) [physics.ins-det]. URL: <https://arxiv.org/abs/2601.10807>.
- [5] J Isberg et al. “Charge collection distance measurements in single and polycrystalline CVD diamond”. In: *Diamond and related materials* 13.4-8 (2004), pp. 872–875.
- [6] S. Spannagel et al. “Allpix2: A modular simulation framework for silicon detectors”. In: *Nuclear Instruments and Methods in Physics Research Section A: Accelerators, Spectrometers, Detectors and Associated Equipment* 901 (2018), pp. 164–172. ISSN: 0168-9002. DOI: <https://doi.org/10.1016/j.nima.2018.06.020>.
- [7] Florian Robert Kassel. “The rate dependent radiation induced signal degradation of diamond detectors”. PhD thesis. Dissertation, Karlsruhe, Karlsruher Institut für Technologie (KIT), 2017, 2017.
- [8] Takehiro Shimaoka et al. “Fano factor evaluation of diamond detectors for alpha particles”. In: *physica status solidi (a)* 213.10 (2016), pp. 2629–2633.
- [9] Karl Hecht. “Zum Mechanismus des lichtelektrischen Primärstromes in isolierenden Kristallen”. In: *Zeitschrift für Physik* 77.3 (1932), pp. 235–245.
- [10] Lukas Báni et al. “A study of the radiation tolerance of cvd diamond to 70 mev protons, fast neutrons and 200 mev pions”. In: *Sensors* 20.22 (2020), p. 6648.
- [11] Faiz Rahman Ishaqzai et al. *Compiled drift-velocity and mobility data for charge carriers in diamond*. TUDodata research data repository, TU Dortmund University. 2025. DOI: [10.17877/TUDODATA-2025-MIESBVSJ](https://doi.org/10.17877/TUDODATA-2025-MIESBVSJ). URL: <https://doi.org/10.17877/TUDODATA-2025-MIESBVSJ>.
- [12] CIVIDEC Instrumentation. *Cx-L Spectroscopic Amplifier*. <https://cividec.at/electronics-Cx-L.html>. Accessed: 2026-03-06.
- [13] Tektronix, Inc. *Mixed Signal Oscilloscopes: MSO5000B, DPO5000B Series Datasheet*. <https://www.testequipmenthq.com/datasheets/TEKTRONIX-MSO5204B-Datasheet.pdf>. Accessed: 2026-03-06. Mar. 2018.
- [14] Faiz Ur Rahman Ishaqzai et al. *Charge collection distance measurements for a diamond detector using a strontium-90 source*. Version DRAFT VERSION. 2026. DOI: [10.17877/TUDODATA-2026-ODJ7MD](https://doi.org/10.17877/TUDODATA-2026-ODJ7MD). URL: <https://doi.org/10.17877/TUDODATA-2026-ODJ7MD>.
- [15] CIVIDEC Instrumentation. *C2-TCT TCT Amplifier, 10 kHz - 2 GHz, 40 dB*. <https://cividec.at/electronics-C2-TCT.html>. Accessed: 2026-03-06.
- [16] Particulars, Advanced Measurement Systems. *Particulars Wide Band Current Amplifiers*. <https://www.particulars.si/downloads/ParticularsAmps-Manuals.pdf>. Accessed: 2026-03-06. Mar. 2017.
- [17] H. Pernegger et al. “Charge-carrier properties in synthetic single-crystal diamond measured with the transient-current technique”. In: *Journal of Applied Physics* 97 (7 Apr. 2005). ISSN: 00218979. DOI: [10.1063/1.1863417](https://doi.org/10.1063/1.1863417).
- [18] Michal Pomorski et al. “Electronic properties of single crystal CVD diamond and its suitability for particle detection in hadron physics experiments”. In: *Wolfgang von Goethe University, Frankfurt am Main, Germany* (2008).
- [19] Markus Gabrysch et al. “Electron and hole drift velocity in chemical vapor deposition diamond”. In: *Journal of Applied Physics* 109 (6 Mar. 2011). ISSN: 00218979. DOI: [10.1063/1.3554721](https://doi.org/10.1063/1.3554721).
- [20] Hendrik Jansen et al. “Temperature dependence of charge carrier mobility in single-crystal chemical vapour deposition diamond”. In: *Journal of Applied Physics* 113 (17 May 2013). ISSN: 00218979. DOI: [10.1063/1.4802679](https://doi.org/10.1063/1.4802679).
- [21] M. Pomorski et al. “Characterization of the charge-carrier transport properties of Ila-Tech SC diamond for radiation detection applications”. In: *Physica Status Solidi (A) Applications and Materials Science* 212 (11 Nov. 2015), pp. 2553–2558. ISSN: 18626319. DOI: [10.1002/pssa.201532230](https://doi.org/10.1002/pssa.201532230).
- [22] R Wallny et al. “Recent progress in CVD diamond detector RD The RD42 Collaboration”. In: *The 28th International Workshop on Vertex Detectors, Vertex 2019*. Proceedings of Science, Sept. 2020. URL: <https://pos.sissa.it/>.
- [23] G. Bassi et al. “Calibration of diamond detectors for dosimetry in beam-loss monitoring”. In: *Nuclear Instruments and Methods in Physics Research, Section A: Accelerators, Spectrometers, Detectors and Associated Equipment* 1004 (July 2021). ISSN: 01689002. DOI: [10.1016/j.nima.2021.165383](https://doi.org/10.1016/j.nima.2021.165383).
- [24] Konstantin Zyablyuk et al. “Polarization and depolarization control of single crystal CVD diamond detectors by UV and visible light illumination”. In: *Nuclear Instruments and Methods in Physics Research, Section A: Accelerators, Spectrometers, Detectors and Associated Equipment* 1042 (Nov. 2022). ISSN: 01689002. DOI: [10.1016/j.nima.2022.167461](https://doi.org/10.1016/j.nima.2022.167461).
- [25] A. Portier et al. “Carrier Mobility up to 106 cm² V⁻¹ s⁻¹ Measured in Single-Crystal Diamond by the Time-of-Flight Electron-Beam-Induced-Current Technique”. In: *Physical Review Applied* 20 (2 Aug. 2023). ISSN: 23317019. DOI: [10.1103/PhysRevApplied.20.024037](https://doi.org/10.1103/PhysRevApplied.20.024037).
- [26] Muhammad Jauhar Kholili et al. “Transient-Current Technique Characterization of Diamond Detector and Proposal of a Diamond Detector with Charge Amplification”. In: *Physica Status Solidi (A) Applications and Materials Science* 221 (4 Feb. 2024). ISSN: 18626319. DOI: [10.1002/pssa.202300673](https://doi.org/10.1002/pssa.202300673).
- [27] L Reggiani et al. “Hole-drift velocity in natural diamond”. In: *Physical Review B* 28 (6 Mar. 1981).
- [28] Miloš Nesladek et al. “Charge transport in high mobility single crystal diamond”. In: *Diamond and Related Materials* 17 (7-10 July 2008), pp. 1235–1240. ISSN: 09259635. DOI: [10.1016/j.diamond.2008.03.015](https://doi.org/10.1016/j.diamond.2008.03.015).
- [29] E Berdermann et al. “Progress in detector properties of heteroepitaxial diamond grown by chemical vapor deposition on Ir/YSZ/Si (001) wafers”. In: *Diamond and Related Materials* 97 (2019), p. 107420.